EUROPEAN ORGANIZATION FOR NUCLEAR RESEARCH
European Laboratory for Particle Physics

Large Hadron Collider Project

LHC Project Report 77

2d Finite-Element Calculation of Superconducting Magnets Applying a Reduced Vector Potential Formulation

C. Paul, S. Russenschuck
K. Preis*

Abstract

The program package ROXIE has been developed at CERN for the design and optimization of the coil geometries for the superconducting magnets for the Large Hadron Collider, LHC. It has recently been extended, in a close collaboration with the University of Graz, to the calculation of iron induced effects applying a reduced vector potential formulation. The method allows accurate computation of the multipole errors in the magnets and allows the distinction between the effects resulting from the coil geometry and the yoke geometry.

LHC
*Technical University of Graz, Austria

7th International IGTE Symposium on Numerical Field Calculation in Electrical Engineering and Team Workshop, Sept. 23-26 1996, Graz, Austria

CERN
CH - 1211 Geneva 23
Switzerland

Geneva, 23/10/96

2d Finite-Element Calculation of Superconducting Magnets Applying a Reduced Vector Potential $\vec{A}_r$-Formulation

C.Paul*, K. Preis+, S. Russenschuck*,
* CERN, Geneva, Switzerland
+ Technical University of Graz, Austria

Abstract: The program package ROXIE has been developed at CERN for the design and optimization of the coil geometries for the superconducting magnets for the Large-Hadron-Collider, LHC. It has recently been extented, in a close collabortion with the University of Graz, to the calculation of iron induced effects applying a reduced vector potential formulation. The method allows accurate computation of the multipole errors in the magnets and allows the distinction between the effects resulting from the coil geometry and the yoke geometry.

I. Introduction

The Large Hadron Collider (LHC) project is a superconducting accelerator for protons, heavy ions and electron-proton collisions in the multi-TeV energy range to be installed at CERN. In order to achieve the design energy within the constraint of the existing LEP tunnel with a circumference of about 27 km, the magnet system must operate in superfluid helium below 2K. Space limitations in the tunnel as well as cost considerations dictate a two-in-one magnet design, where the two rings are incorporated into the same cryostat. The main dipole magnets will operate at about 0.58 T at injection and 8.40 T at nominal current (magnetic length in cold conditions 14.2 m) and the quadrupoles at 220 T/m field gradient (magnetic length 3.0 m) [3]. The superconducting magnets are characterized by the dominance of the coil geometry for the field distribution. For the optimization of the magnet, contradictory parameters such as maximum dipole field, minimum content of unwanted multipoles and sufficient safety margin for the conductor must be considered. The keystoning of the conductors and the grading of the current densities between the two layers make necessary a computational method that allows to model the coil and calculate the excitational field with a higher accuracy than rendered by commercial FE packages. In addition the characteristic data for both the coil and the iron configuration has to be parametric for the application of mathematical optimization techniques. The program package ROXIE [5] has been developed at CERN for the design and optimization of the coil geometries for the superconducting magnets for the Large-Hadron-Collider, LHC. It has recently been extended, in a close collaboration with the University of Graz, to the calculation of iron induced effects applying a reduced vector potential formulation.

II. The reduced vector potential formulation

Here, the emphasis is put on the principle idea, the comparison to the total vector potential, and the main advantage of this method for the calculation of fields in superconducting magnets. With the governing Maxwell equations for magnetostatics $\bigtriangledown \times \vec{H} = \vec{J}$, $\bigtriangledown \cdot \vec{B} = 0$ in region Ω, coupled through the material equations $\vec{B} = \mu\vec{H}$ resp. $\vec{H} = \nu\vec{B}$ together with the following boundary conditions;

$$\vec{H} \times \vec{n} = \vec{K} \quad \text{on } \Gamma_H \tag{1}$$

$$\vec{B} \cdot \vec{n} = -b_m \quad \text{on } \Gamma_B \tag{2}$$

where $\vec{K}$ is the surface current and b_m is a fictitious magnetic charge density on the boundary Γ of the region Ω, we can set $\vec{B} = \bigtriangledown \times \vec{A}$ and it follows

$$\bigtriangledown \times \nu \bigtriangledown \times \vec{A} = \vec{J} \tag{3}$$

where $\vec{J}$ is the current density. In order to make the vector potential $\vec{A}$ unique it is necessary to define its divergence and, on the boundary Γ, either its normal component or its tangential component. By introducing the Coulomb gauge described in [1] and merging both differential equations the complete $\vec{A}$-formulation with its boundary conditions reads:

$$\bigtriangledown \times \nu \bigtriangledown \times \vec{A} - \bigtriangledown \nu \bigtriangledown \cdot \vec{A} = \vec{J} \text{ in } \Omega, \tag{4}$$

$$\nu \bigtriangledown \times \vec{A} \times \vec{n} = \vec{K} \text{ on } \Gamma_H, \tag{5}$$

$$\vec{A} \cdot \vec{n} = 0 \text{ on } \Gamma_H, \tag{6}$$

$$\vec{n} \times \vec{A} = \vec{\alpha} \text{ on } \Gamma_B, \tag{7}$$

$$\nu \bigtriangledown \cdot \vec{A} = 0 \text{ on } \Gamma_B. \tag{8}$$

The current density $\vec{J}$ appears on the right hand side of the differential equation of the $\vec{A}$-formulation. The consequence of this is that using the finite element method for the solution of this problem the relatively complicated shape of the coils has to be modelled in the FE-mesh. Thus

the goal is to replace $\vec{J}$ in a way that it does not explicitly appear in the finite element equation system. Therefore, the vector potential $\vec{A}$ is split into parts

$$\vec{A} = \vec{A_s} + \vec{A_r} \tag{9}$$

where $\vec{A_r}$ is the reduced vector potential due to the magnetisation and $\vec{A_s}$ is the impressed vector potential due to the source currents in free space. The relationship between the impressed vector potential $\vec{A_s}$ and the field vector $\vec{H_s}$ is,

$$\bigtriangledown \times \vec{A_s} = \mu_0 \vec{H_s} \tag{10}$$

and for conductor source regions with current density $\vec{J_s}$ the field vector $\vec{H_s}$ is given by Biot-Savart's Law [6]

$$\vec{H_s} = \frac{1}{4\pi} \int_{\Omega} \vec{J_s} \times \bigtriangledown (\frac{1}{R})\, d\Omega \tag{11}$$

where $R = \mid r_q - r_a \mid$ is the distance from the source point r_q to the field point r_a. The field equations in terms of a reduced vector potential $\vec{A_r}$ then differ for the iron region Ω_i and the air region Ω_a where the sources (coils) are located. Following the same procedure as for the total potential leads to [4]:

$$\bigtriangledown \times \nu \bigtriangledown \times \vec{A_{r_i}} - \bigtriangledown \nu \bigtriangledown \cdot \vec{A_{r_i}} = - \bigtriangledown \times \nu \bigtriangledown \times \vec{A_s} \quad \text{in } \Omega_i \tag{12}$$

$$\bigtriangledown \times \nu_0 \bigtriangledown \times \vec{A_{r_a}} - \bigtriangledown \nu_0 \bigtriangledown \cdot \vec{A_{r_a}} = 0 \quad \text{in } \Omega_a. \tag{13}$$

Taking the curl of Eq. (10) gives $\bigtriangledown \times \nu_0 \bigtriangledown \times \vec{A_s} = \bigtriangledown \times \vec{H_s}$, which represents the current density $\vec{J_s}$. At this stage it is sufficient to show the complete $\vec{A_r}$-formulation where the surface current density $\vec{K}$ and the fictive magnetic charge density b_m are assumed to be zero:

$$\bigtriangledown \times \nu \bigtriangledown \times \vec{A_{r_i}} - \bigtriangledown \nu \bigtriangledown \cdot \vec{A_{r_i}} = - \bigtriangledown \times \nu \bigtriangledown \times \vec{A_s} \quad \Omega_i \tag{14}$$

$$\bigtriangledown \times \nu_0 \bigtriangledown \times \vec{A_{r_a}} - \bigtriangledown \nu_0 \bigtriangledown \cdot \vec{A_{r_a}} = 0 \quad \Omega_a \tag{15}$$

$$\nu \bigtriangledown \times \vec{A_{r_i}} \times \vec{n} = 0 \quad \Gamma_{H_i} \tag{16}$$

$$\vec{A_{r_i}} \cdot \vec{n} = 0 \quad \Gamma_{H_i} \tag{17}$$

$$\vec{n} \times \vec{A_{r_i}} = 0 \quad \Gamma_{B_i} \tag{18}$$

$$\nu \bigtriangledown \cdot \vec{A_{r_i}} = 0 \quad \Gamma_{B_i} \tag{19}$$

$$\nu_0 \bigtriangledown \times \vec{A_{r_a}} \times \vec{n} = 0 \quad \Gamma_{H_a} \tag{20}$$

$$\vec{A_{r_a}} \cdot \vec{n} = 0 \quad \Gamma_{H_a} \tag{21}$$

$$\vec{n} \times \vec{A_{r_a}} = 0 \quad \Gamma_{B_a} \tag{22}$$

$$\nu_0 \bigtriangledown \cdot \vec{A_{r_a}} = 0 \quad \Gamma_{B_a} \tag{23}$$

and along the interface Γ_{ai} between the iron and air region

$$(\nu_0 \bigtriangledown \times \vec{A_{r_a}} + \nu_0 \bigtriangledown \times \vec{A_s}) \times \vec{n_a} + (\nu \bigtriangledown \times \vec{A_{r_i}} + \nu \bigtriangledown \times \vec{A_s}) \times \vec{n_i} = 0. \tag{24}$$

Applying Ritz's procedure results in a volume integral in the iron region Ω_i and a surface integral on the boundary between iron and air:

$$\int_{\Omega_i} (\nu \bigtriangledown \times \vec{A_{r_i}} \cdot \bigtriangledown \times \vec{f_k} + \nu \bigtriangledown \cdot \vec{A_{r_i}} \bigtriangledown \cdot \vec{f_k})\, d\Omega + \int_{\Omega_a} (\nu_0 \bigtriangledown \times \vec{A_{r_a}} \cdot \bigtriangledown \times \vec{f_k} + \nu_0 \bigtriangledown \cdot \vec{A_{r_a}} \bigtriangledown \cdot \vec{f_k})\, d\Omega = \int_{\Gamma_{ai}} (\vec{f_k} \cdot \nu_0 \bigtriangledown \times \vec{A_s} \times \vec{n_i})\, d\Gamma - \int_{\Omega_i} (\nu \bigtriangledown \times \vec{A_s} \cdot \bigtriangledown \times \vec{f_k})\, d\Omega \tag{25}$$

Because of Eq. (10) the curl of $\vec{A_s}$ has not to be computed as $\vec{H_s}$ is given by Biot-Savart's law and can be included directly in the right hand side of Eq. (25).

III. Field components

The expansion of the complex field $B_y + iB_x$ in the plane $z = x + iy$ is performed for field calculations and measurements as follows [2]:

$$B_y + iB_x = \sum_{n=1}^{\infty} (B_n + iA_n) z^{n-1} \tag{26}$$

with $z = x + iy = re^{i\varphi} = r(\cos\varphi + i \sin\varphi)$ and $B_\varphi + iB_r = (B_y + iB_x)e^{i\varphi}$ we get

$$B_r = \sum_{n=1}^{\infty} r^{n-1} (B_n \sin n\varphi + A_n \cos n\varphi). \tag{27}$$

If the field is expanded relative to the main field component $B(r_0)$ at $r = r_0$ we get

$$B_y + iB_x = B(r_0) \sum_{n=1}^{\infty} (b_n + ia_n)(z/r_0)^{n-1} \tag{28}$$

and thus

$$B_r = B(r_0) \sum_{n=1}^{\infty} (r/r_0)^{n-1} (b_n \sin n\varphi + a_n \cos n\varphi). \tag{29}$$

The B_n are called the normal and the A_n the skew components of the field, b_n and a_n are the normal and skew relative field components. In ROXIE the r- component of the field at a given radius $r = r_0$ is harmonically analyzed by means of the program TRICOF from the CERN Library. With A being usually defined as the coefficients of the cos terms and B being the coefficients of the sin terms we get from given equidistant function values in the interval $-\pi \le \varphi \le \pi$:

$$B_r(r_0) = \sum_{n=1}^{\infty} (B_{n(r_0)} \sin n\varphi + A_{n(r_0)} \cos n\varphi) \tag{30}$$

$$= B_1(r_0) \sum_{n=1}^{\infty} (b_n \sin n\varphi + a_n \cos n\varphi). \tag{31}$$

which is in agreement with Eq. (29) for the unit radius. Note that for a positive skew component B_r is positive on the x-axis.

IV. The main-dipole geometry

The following results are given for a dipole coil design (drawing no. 06LHCMB-T-00010) which was optimized for a part compensation of the b_5 ,b_7, and b_9 components resulting from persistent currents at injection. During ramp of the superconducting magnets from 0.58 to 8.4 T nominal dipole field additional currents, the persistent currents, are induced in the filaments. These currents persist for a long time as they decay only through flux creep. At injection they were estimated to be $b_3 = -4.1667$, $b_5 = +0.2073$ and $b_7 = -0.0357$ (in units of 10^-4 at radius 10 mm) [7].

Fig. (1) shows the coil cross-section. Note that due to insufficient keystoning of the cable the blocks do not follow the curvature of circles on the outer diameter of the coils.

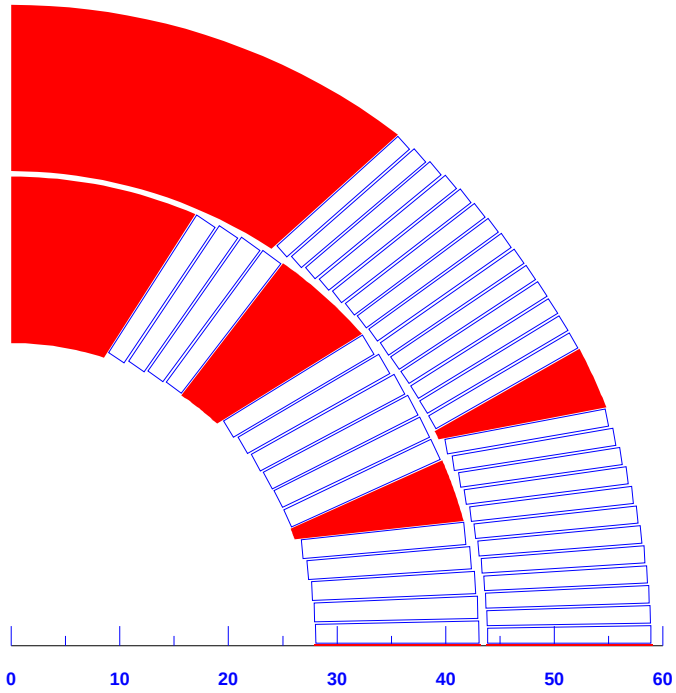

Figure 1: Coil with optimized block positions for part compensation of the persistent current multipole errors at injection, size in mm

For the yoke the drawing 06LHCMBP-N10070 for the warm laminations was given and the cold dimensions were calculated. Note that the beam separation distance is 194 mm in cold conditions. This assumption would leave the yoke laminations unchanged with respect to the present drawings. Fig. (2) shows a sketch of the yoke with the symbols used in the ROXIE input file. All these dimensions can be addressed as design variables for a subsequent yoke optimization or fine-tuning. The dipole geometry with coil and iron yoke is displayed in Fig. (3).

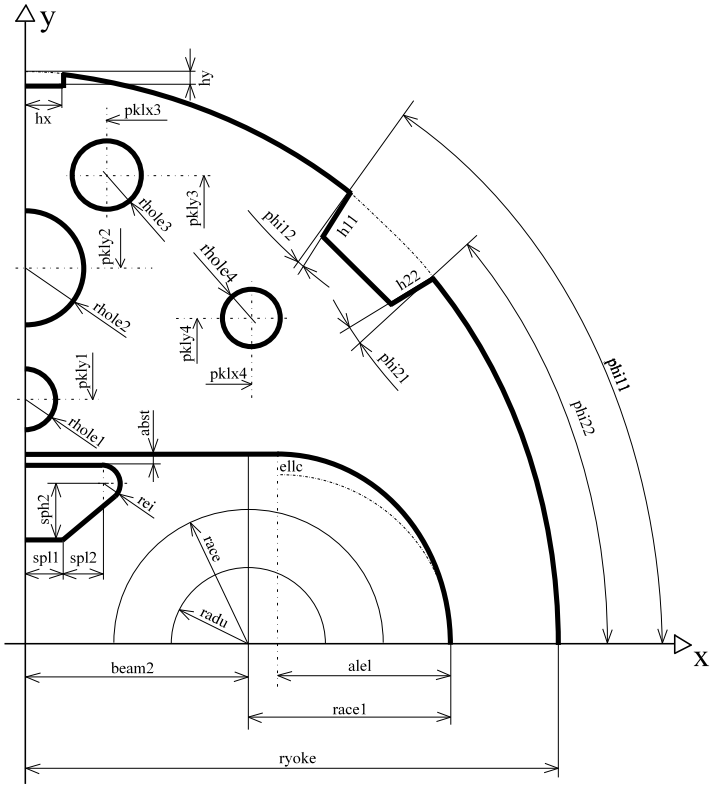

Figure 2: Symbolic input data for the main dipole geometry

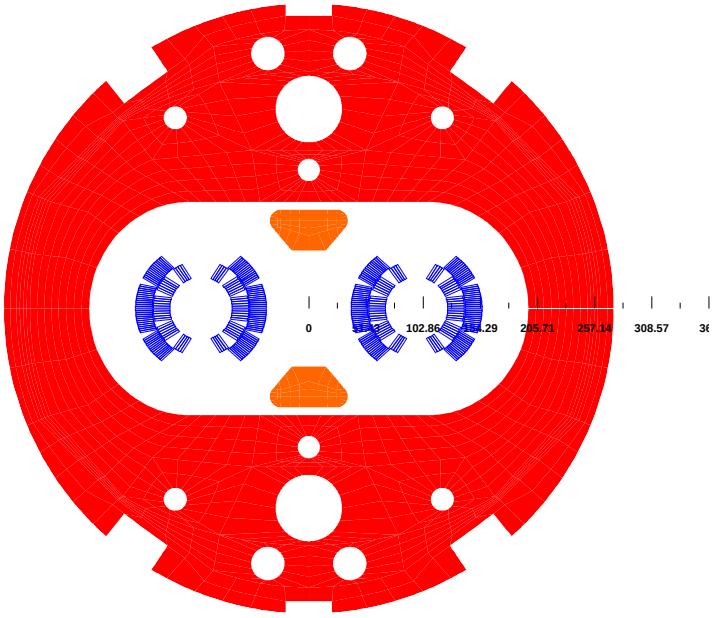

Figure 3: Geometric model of main dipole cold mass

Table 1: Relative multipole errors in units of 10^{-4} at radius 10 mm as a function of the mesh size at normal operation 8.4 T for the main dipole without vacuum vessel. The far field boundary is at 5 times the yoke outer diameter.

	Number of nodes			
	1800	7200	28500	36000
n	b_n	b_n	b_n	b_n
2	1.19320	1.27823	1.28336	1.28377
3	-0.21129	-0.24245	-0.23930	-0.23928
4	-0.14697	-0.14834	-0.14867	-0.14875
5	-0.20487	-0.18869	-0.18650	-0.18650
6	0.01211	0.00060	0.00060	0.00067
7	-0.06011	0.03308	0.03381	0.03380
8	0.02150	-0.00040	0.00003	0.00002
9	0.06972	-0.00338	-0.01025	-0.01026
10	-0.00654	0.00003	0.00000	0.00009
11	-0.00996	0.01680	0.00771	0.00769

V. Numerical Accuracy

Table (1) shows the calculated multipole content for the LHC main dipole for different numbers of elements in the finite-element mesh using eight-noded, isoparametric second order elements. The results show convergence for meshes bigger than 28500 nodes. The higher order multipoles b_7, b_9, b_{11} are hardly influenced by the yoke and the iron saturation effect. The estimates for a coil in an infinite permeable iron yoke are $b_7 = 0.034$, $b_9 = -0.010$, and $b_{11} = 0.0088$. These multipoles are therefore a good measure of the accuracy of the field solution. The quadrupole component that arises from the two-in-one geometry is relatively insensitive to the mesh size.

Table (2) shows the calculated multipole content for the LHC main dipole depending on the far field boundary conditions. The boundary was chosen to be 1.1, 5., and 10. times the radius of the cold mass. The result shows that the higher order multipoles are not dependent on the boundary whereas the iron induced quadrupole component and the sextupole component can be used as a measure for the accuracy of the solution. A boundary which is at least 5 times the radius of the cold mass is appropriate. At the symmetry planes x=0, and y=0 the Neumann boundary condition imposes the flux to be normal to the surfaces. In the vector potential formulation they are natural conditions which are satisfied in the weak sense only. The accuracy can be improved by refining the discretization in the vicinity of the symmetry planes. The B_t components at this planes can therefore be considered as a measure of the satisfaction of the boundary conditions and is in our case in the order of $10^{-7}T$.

Due to the keystoning of the superconducting cable the current density is higher at the narrow side of the cable. This effect cannot be neglected as the sextupole field component changes. Table (3) shows the results for the case with a grading of the current density and for the case where the grading is not considered. The difference is an offset of the sextupole component of about 0.6 units. The saturation effects are the same, as the excitational field in the iron does not change very much with this grading. Therefore also the quadrupole components that are due to the two- in-one design show only minimal dependecy on the grading. If the coils cannot be modelled sufficiently accuratly as is the case in most of the commercially available FE-packages, the sextupole component may contain a relatively large error.

Table 2: Relative multipole errors in units of 10^{-4} at radius = 10 mm and nominal operation, depending on the far field boundary, 28500 nodes.

	Distance of far field boundary		
	1.1 × ryoke	5.0 × ryoke	10.0 × ryoke
n	b_n	b_n	b_n
1	-8.40231 T	-8.36833 T	-8.36815 T
2	2.36867	1.28336	1.27138
3	-0.13080	-0.23930	-0.24019
4	-0.13138	-0.14867	-0.14885
5	-0.18591	-0.18650	-0.18651
6	0.00067	0.00060	0.00060
7	0.03378	0.03381	0.03381
8	0.00004	0.00003	0.00003
9	-0.01024	-0.01025	-0.01025
10	0.00000	0.00000	0.00000
11	0.00773	0.00771	0.00770

Table 3: Relative multipole errors in units of 10^{-4} considering the grading of the current density in the superconducting cable compared to the results with no grading (radius = 10 mm). Main dipole without vacuum vessel

	At injection, 0.58T		At nom. operation, 8.4T	
	without grading	with grading	without grading	with grading
n	b_n	b_n	b_n	b_n
2	-0.25362	-0.24612	1.24352	1.28336
3	-0.12407	-0.71274	0.39358	-0.23930
4	-0.11136	-0.11050	-0.14982	-0.14867
5	-0.18642	-0.17652	-0.19540	-0.18650
6	0.00185	0.00183	0.00056	0.00060
7	0.03782	0.03556	0.03836	0.03381
8	-0.00002	-0.00002	-0.00002	0.00003
9	-0.01006	-0.01056	-0.01017	-0.01025
10	0.00002	0.00002	0.00001	0.00001
11	0.00662	0.00704	0.00693	0.00771

VI. Results

Fig. (4) shows the lower order harmonics as a function of the main field. About -0.7 units of sextupole result

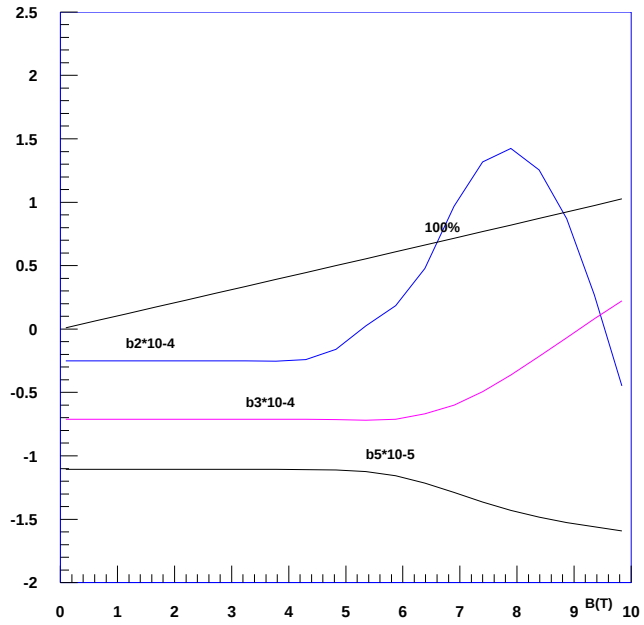

Figure 4: Variation of the relative (lower order) multipole errors with main field calculated for main dipole without vacuum vessel; together with the percentage on the load-line given for block no. 5

from the iron geometry. Sextupole and quadrupole harmonics depend on saturation effects. Fig. (5) and Fig. (6) show the physical explanation of the measures taken in order to minimize the variation of these multipoles. The quadrupole component results from the two-in-one design and the flux being divided into two paths, one across the mid-plane x=0 into the second aperture and one across the y=0 into the lower half of the yoke. The small hole in the mid-plane helps to balance the flux in the two paths, one across the mid plane into the second aperture and the second along the yoke leg across the $y = 0$ plane. The effect of this hole vanishes with saturation but the second hole between the heat exchanger tube and the outer yoke radius leads to local saturation effects at nominal current thus balancing the flux in the two paths.

The vacuum vessel being off-centered with respect to the magnet horizontal axis introduces some skew dipole and skew quadrupole components that get more and more pronounced at fields higher than 7 T as can be seen from Fig. 7. The vacuum vessel also has an influence on the variation of the normal quadrupole which increases and is then about 2 units at 8.4 T. Sextupole and higher order multipoles are basically not affected. Table (4) gives the multipoles at injection and nominal field level.

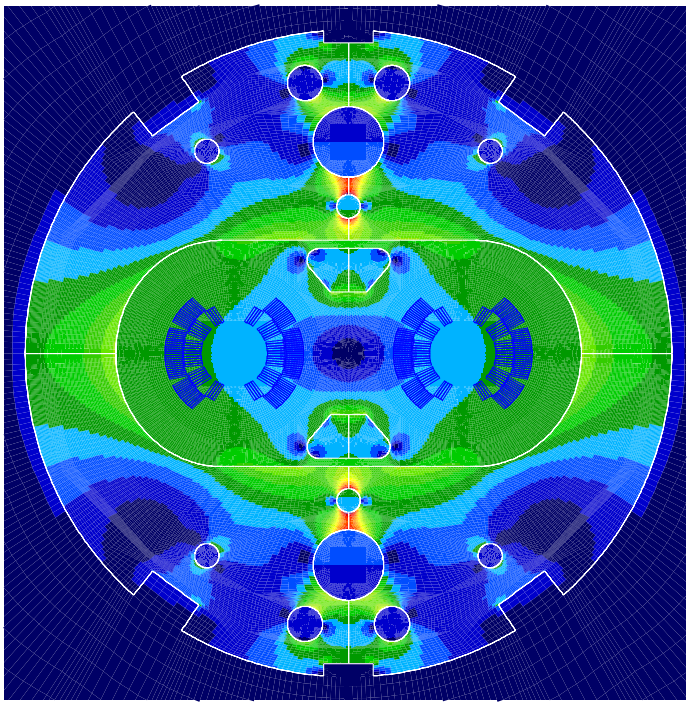

Figure 5: Modulus of reduced field resulting from iron magnetization only, given for injection field level of 0.58 T

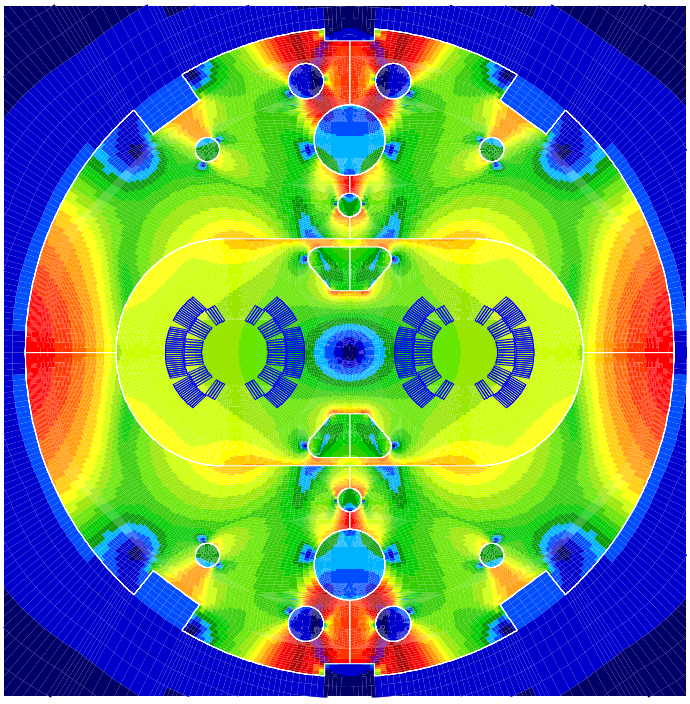

Figure 6: Modulus of reduced field at nominal operation, field level of 8.4 T in the aperture

Table 4: Relative multipole errors in units of 10^{-4} at radius 10 mm for the main dipole in an symmetric and asymmetric vacuum vessel 12 mm thickness and 80 mm off-centering with respect to cold mass

	At injection, 0.58T		At nom. operation, 8.4T	
n	b_n	a_n	b_n	a_n
1		0.00003		0.59679
2	-0.24788	0.00000	2.00362	-0.06635
3	-0.71298	0.00000	-0.14884	0.00542
4	-0.11049	-0.00002	-0.13595	-0.00024
5	-0.17651	0.00000	-0.18474	0.00001
6	0.00183	0.00000	0.00064	0.00000
7	0.03555	0.00000	0.03597	0.00000
8	-0.00002	-0.00002	-0.00002	-0.00001
9	-0.01055	0.00000	-0.01065	0.00000
10	0.00002	0.00000	0.00001	0.00000
11	0.00703	0.00000	0.00737	0.00000

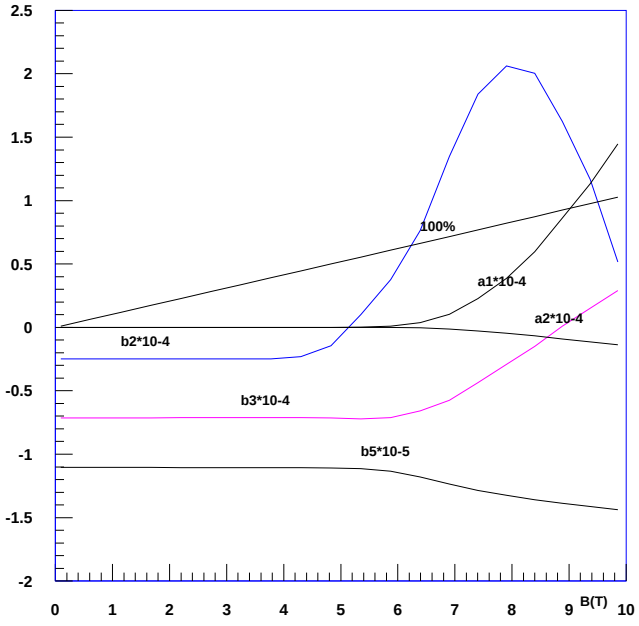

Figure 7: Variation of lower order multipole errors with main field given for the main dipole in its asymmetric vacuum vessel.

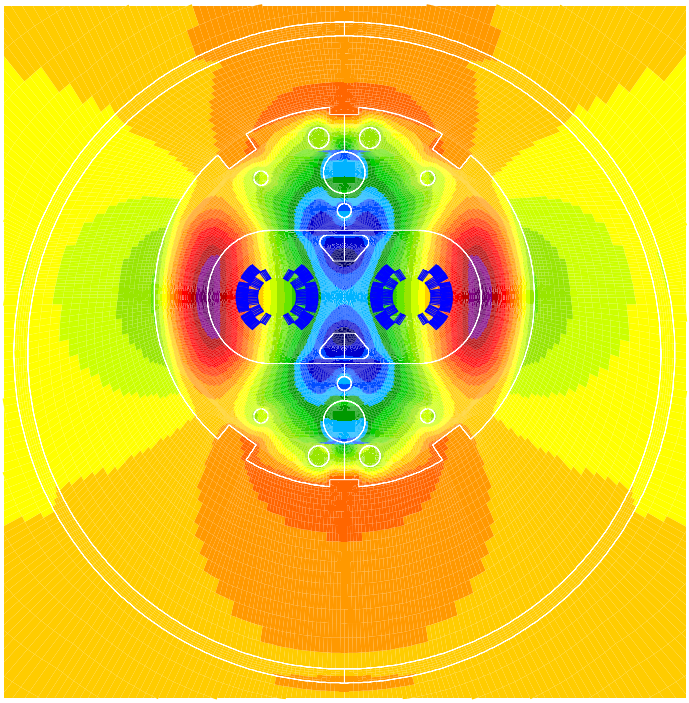

Figure 8: Reduced vector potential for main dipole in asymmetric vacuum vessel

The big advantage of the new program is that the coils have not to be meshed and therefore asymmetries caused by deformations or shifts of the coil blocks can easily be calculated. As an example, the effects resulting from a vertical (y direction) off-centering of the coils with respect to the yoke are calculated. The coil was shifted by 0.05 mm in an upward direction. As expected, the main effect is on the skew quadrupole of about -0.17 units at injection. Interesting is the reduction of these errors with excitation because of the different saturation in the upper and lower yoke halves. At nominal field the skew quadrupole is -0.11 units.

Fig. (9) shows the fringing field at a radius of 290 mm outside the cold mass as a function of the angular position, -90 deg. is the bottom of the magnet, 90 deg. the top.

As the reduced field coming from the iron magnetization and the excitational field from the coil can be calculated separately it is also possible to calculate the peak field in the coils which determines the margin to quench with an higher accuracy than before. Fig. 10 shows the load line curves for the coil blocks of the main dipole magnet. Blocks 1 and 2 are in the outer layer, block 3 - 5 are the inner layer blocks.

The point J_c, B_c is derived from solving the equations

$$B_c = \lambda_1 \cdot B = B_{ref} + \lambda_2 \tag{32}$$

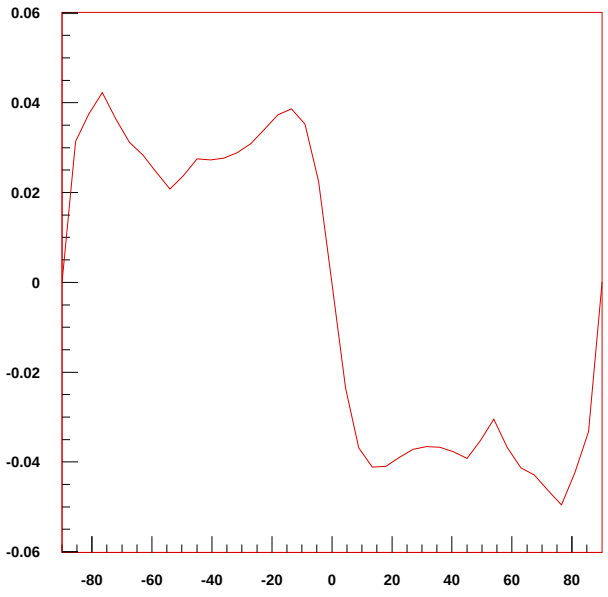

Figure 9: Radial component of the fringing field (in T) outside the cold bore at a radius of 290 mm, given for the main dipole in its asymmetric vacuum vessel. (-90 deg. is the bottom of the magnet, 90 deg. at the top.)

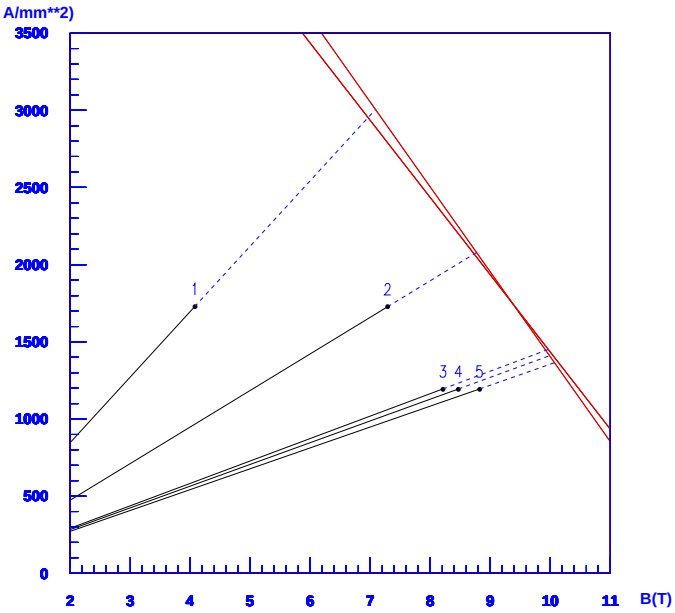

Figure 10: Load line for the main dipole. Blocks 1 and 2 are in the outer layer, 3 - 5 are the inner layer coil blocks

$$J_c = \lambda_1 \cdot J = J_c(B_{ref}) + \lambda_2 \frac{dJ_c}{dB} \tag{33}$$

The current density in the superconductor is given by

$$J_{sc} = \frac{I_{cable}}{A_{sc}} = \frac{I_{cable} \cdot (1 + \frac{Cu}{Sc})}{n \cdot \frac{d^2 \cdot \pi}{4}} \tag{34}$$

where I_{cable} is the total current in the cable, n is the number of strands in the cable and d is the strand diameter. From the critical current density J_c and dJ_c/dB the percentage of the critical current density in the working point can be evaluated. The short sample $B - J$ characteristic curves are approximated by

$$J_{sc} = -\frac{dJ_c}{dB} \cdot B + J_c \tag{35}$$

at 1.9 Kelvin. The assumptions of the cable characteristics were: Inner layer; $T_{ref} = 1.9$ K, $B_{ref} = 10$ T, $J_c(B_{ref}) = 1433.3$ A/mm**2 , $\frac{dJ_c}{dB} = 500.34$ A/mm**2 T . Outer layer: $T_{ref} = 1.9$ K, $B_{ref} = 9$ T, $J_c(B_{ref}) = 1953.0$ A/mm**2 , $\frac{dJ_c}{dB} = 550.03$ A/mm**2 T.

Figures (4) and (7) show the mutlipole content versus excitation. Also the percentage on the load line, calculated for the block with the highest peak field (block No. 5), is displayed. The short sample field Bss for the dipole magnet in its off-centered cryostat is estimated to be 9.6 T. The peak-field to main-field ratio for the block No. 5 with the least margin to quench is 1.053.

VII. References

[1] O. Biro and K. R. Richter. *CAD in Electromagnetism*, volume 82 of *Advances in Electronics and Electron Physics*, pages 1 – 96. Academic Press, 1991.

[2] The LHC Study Group. *The Yellow Book, LHC - The Large Hadron Collider - Conceptual Design.* CERN/AC/95-5(LHC), 1995.

[3] R. Perin. Superconducting magnets. *LHC Note 319*, 1995.

[4] K. Preis, I. Bardi, O. Biro, C. Magele, W. Renhart, K. R. Richter, and G. Vrisk. Numerical analysis of 3d magnetostatic fields. *IEEE Trans. on Magnetics*, 27(5):3798 – 3803, 1991.

[5] S. Russenschuck. Synthesis, inverse problems and optimization in computational electromagnetics. *Int. Journal of Numerical Modelling: Electronic Networks, Devices and Fields*, 9:45 – 57, 1996.

[6] K. Simonyi. *Theoretische Elektrotechnik.* VEB Deutscher Verlag der Wissenschaften, Berlin, 10 edition, 1993.

[7] R. Wolf. *Private communications.* CERN/LHC-MMS.